

Novel three-dimensional Fermi surface and electron-correlation-induced charge density wave in FeGe

Lin Wu, Yating Hu, Di Wang,* and Xiangang Wan†

National Laboratory of Solid State Microstructures and School of Physics, Nanjing University, Nanjing 210093, China and Collaborative Innovation Center of Advanced Microstructures, Nanjing University, Nanjing 210093, China

(Dated: February 8, 2023)

As the first magnetic kagome material to exhibit the charge density wave (CDW) order, FeGe has attracted much attention in recent studies. Similar to AV_3Sb_5 ($A = K, Cs, Rb$), FeGe exhibits the CDW pattern with an in-plane 2×2 structure and the existence of van Hove singularities (vHSs) near the Fermi level. However, sharply different from AV_3Sb_5 which has phonon instability at M point, all the theoretically calculated phonon frequencies in FeGe remain positive. Here, we perform a comprehensive study of the band structures, Fermi surfaces and nesting function of FeGe through first-principles calculations. Surprisingly, we find that the maximum of nesting function is at K point instead of M point. Two Fermi pockets with $Fe-d_{xz}$ and $Fe-d_{x^2-y^2}/d_{xy}$ orbital characters have large contribution to the Fermi nesting, which evolve significantly with k_z , indicating the highly three-dimensional (3D) feature of FeGe in contrast to AV_3Sb_5 . Meanwhile, the vHSs are close to the Fermi surface only in a small k_z range, and does not play a leading role in nesting function. Considering the effect of local Coulomb interaction, we reveal that the Fermi level eigenstates nested by vector K are mainly distributed from unequal sublattice occupancy, thus the instability at K point is significantly suppressed. Meanwhile, the wave functions nested by vector M have many ingredients located at the same Fe site, thus the instability at M point is enhanced. This indicates that the electron correlation, rather than electron-phonon interaction, plays a key role in the CDW transition at M point.

Kagome lattice materials [1–4] exhibit unique electronic structure signatures owing to their unconventional geometric characteristics, embracing the flat bands induced by destructive interference of nearest-neighbour hopping, a pair of van Hove singularities (vHSs) at M point, and Dirac cone dispersion at K point [5–10]. A wide array of exotic physical phenomena in the kagome lattice arises from different degrees of electron filling. When large density of states (DOS) from the kagome flat bands are located near the Fermi level, strong electron correlations can induce magnetic order [5, 6, 11]. Meanwhile, when vHSs are located near the Fermi level, interaction between the saddle points and lattice instability could induce charge density wave (CDW) order with a 2×2 structure in xy-plane [7–10, 12]. Therefore kagome lattice materials serve an essential platform for studying non-trivial topological physics [13–17], CDW order [18–37], superconductivity [38–41], fractional quantum Hall effect [42–44] and quantum anomalous Hall effect (QAHE) [45–50].

As a well-known family of non-magnetic layered kagome compounds, AV_3Sb_5 ($A = K, Cs, Rb$) [18] were reported to host CDW [19–25, 27–34], superconductivity [39–41], giant QAHE [49, 50] and chiral flux phase [35–37]. In this system, vHSs are located near the Fermi level and the phonon spectrum exhibit two imaginary phonon frequencies locating at the Brillouin zone (BZ) boundary (M ($\frac{1}{2}, 0, 0$) and L ($\frac{1}{2}, 0, \frac{1}{2}$) points) [30, 33], which induce an in-plane 2×2 CDW state identified in experiment [20–25]. On the other hand, there are many kagome magnetic materials such as FeSn [51–55], Fe_3Sn_2 [56, 57], Mn_3Sn [14], Mn_3Ge [47, 48] and $Co_3Sn_2S_2$ [15–17]. However, it may be due to the large energy separation between flat bands and vHSs that CDW order and mag-

netic order have not been generally observed simultaneously in one material [58, 59].

Very recently, the discovery of CDW order coexists with magnetic order in the Kagome material FeGe was reported from a joint experimental study of angle-resolved photoemission spectroscopy (ARPES) [58, 60], neutron and x-ray scattering [60–62], scanning tunneling microscopy (STM) [60, 61, 63] and photoemission [61], which offers a fascinating platform to investigate interplay between the CDW and magnetism. FeGe exhibits a sequence of phase transitions: (1) an A-type antiferromagnetism (AFM) phase appears below the high magnetic transition temperature up to $T_c \sim 410K$ [64], (2) a CDW phase [60–63] takes place at $T_{CDW} \sim 100K$ and the system becomes stable in $2 \times 2 \times 2$ superstructure as previously reported in metal AV_3Sb_5 [20–25], and (3) the magnetic moment weakly cants along the c direction, giving a c -axis double cone AFM structure below a lower transition temperature $T_{canting}$ around 60K [65–70]. Subsequent reports reveal that the vHSs in FeGe, which are originally far from Fermi surface in a nonmagnetic system, are brought to the vicinity of Fermi level due to spin exchange splitting of about 1.8eV caused by magnetic order [58–60]. Though FeGe exhibits the existence of vHSs at the M point near the Fermi level similar to AV_3Sb_5 , it is note-worthy that the imaginary phonon around the M point present in AV_3Sb_5 [30, 33] is not observed in the theoretically calculated phonon spectrum of FeGe [58, 62, 63]. Therefore, a comprehensive study of the band structures, Fermi surfaces, nesting function, and the mechanism of CDW transition in kagome FeGe is an emergency issue, which we will address in this work based on first principles study.

In the present work, we perform a detailed analysis of the electronic structure and an investigation on the nesting function of A-type AFM kagome materials FeGe by employing first-principles calculations. We analyse the variation of the

* diwang0214@nju.edu.cn

† xgwan@nju.edu.cn

energy band structure and the Fermi surface for different k_x - k_y planes as k_z changes from 0 to 0.5, and find that the electronic structures of FeGe have strong 3D feature. The positions of vHSs evidently shift as k_z varies, and only in a small k_z range the vHSs are in proximity to Fermi level (± 0.1 eV), distinct from the quasi-two-dimensional structural characteristics of AV_3Sb_5 [31, 33]. Our numerical results show that the maximum of nesting function is at the K point instead of the M point. Whereafter, we find that two pockets have large contribution to the nesting function, which respectively contribute from the d_{xz} orbital and a combination of $d_{x^2-y^2}/d_{xy}$ orbitals. To understand the conflict between the nesting function at the K point and CDW transition at M point, we consider the effect of local Coulomb interaction [71]. We find that the Fermi surface nesting at the K point is ineffective due to different sublattice characters of the band structures, similar with the sublattice mechanism in superconductors [10, 72]. On the other hand, the CDW instability at the M point could be enhanced by the local Coulomb interaction, since the wave functions nested by vector M are mainly distributed from the same Fe site. It implies that the strong 3D Fermi surfaces and local electron correlation play indispensable parts in the CDW transition in FeGe.

We carried out first-principles density functional theory (DFT) calculations by employing the full-potential all-electron code Wien2k [73]. The local spin density approximation (LSDA) [74] was used as the exchange-correlation functional in our calculations for the A-type AFM state. We chose a fine k-mesh of $200 \times 200 \times 100$ in the irreducible BZ to ensure that the nesting function calculated from the eigenvalues is robust to the number of K points. Since our conclusions are quite different from the typical kagome materials such as AV_3Sb_5 [30, 31, 33], we have also used the Vienna ab initio Simulation Package (VASP) [75, 76] with the projector augmented wave (PAW) [77, 78] method to confirm our electronic structure calculations. The results of the two methods are well consistent, and in this paper we present the calculated results from Wien2k.

We start by performing LSDA calculation for FeGe based on the experimental crystal structure (see Appendix A) and A-type AFM ground state [70]. The band structure and the density of states (DOS) (see Appendix B) are basically similar in many aspects to the isostructure FeSn [51–55]. Our calculations reproduce the results of previous studies [58] quite well. The magnetic moment of the Fe ions is estimated to be $1.55 \mu_B$, which is close to the previous experimental value of about $1.72 \mu_B$ [66, 68]. Besides, similar to AV_3Sb_5 [31, 33], we find a pair of vHSs close to Fermi surface on both the $k_z=0$ and 0.5 high symmetric plane as shown in Fig. 6 of Appendix B.

In order to analyse the orbital components of the energy bands, it is important to take the proper local coordinate axis. Since the angle between the orientations of Fe_A , Fe_B , and Fe_C (see Appendix A) to the same nearest neighbour Ge^{out} atom is 120° in the global coordinate, the x/y components of $\text{Fe}_{A/B/C}$ - d orbitals are not equivalent. The suitable local coordinate of Fe_A , Fe_B , and Fe_C we have chosen are shown in Fig. 5(c) of Appendix A, any two of which could be trans-

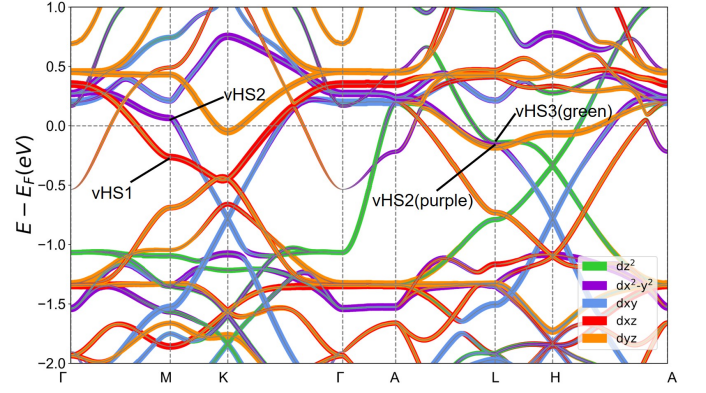


FIG. 1. The orbital-projected electronic band structure of FeGe near Fermi level. The Fe-3d orbital projection is performed with the local coordinate. The orbital characters are labelled by different colors.

formed into each other by the C_3 symmetry operation. The local x-axis always points to the nearest-neighbor Ge^{in} atom and the local z-axis direction is the same as the one in the global coordinate. In this local coordinate, the five Fe-3d orbitals are clearly divided into higher d_{yz} and $d_{x^2-y^2}$ parts and lower d_{z^2} , d_{xz} and d_{xy} parts, consistent with the e_g - t_{2g} relationship in the ortho-octahedral crystal field. The selection of such local coordinate is also helpful to the analysis of the Fermi pockets as shown in the following.

We present the orbital components of the energy bands in Fig. 1 using the above local coordinate. As mentioned above, the kagome lattice with nearest-neighbour hopping will present the typical three-band structure including flat band, vHS, and Dirac cone [5–10]. Along the high symmetry directions $\Gamma - M - K - \Gamma$ lying in $k_z=0$ plane, there are two different kagome structures near the Fermi level. One of the Kagome structures consists of Fe- d_{xz} orbitals, which are located between -2.0 and 0.5 eV, and contain the vHS1 located at -0.26 eV below E_F , as marked in red in Fig. 1. The other kagome structure containing vHS2 consists of a combination of $d_{x^2-y^2}$ and d_{xy} orbitals shown in purple and blue respectively. The vHS2 is located above the Fermi energy (0.07 eV). Three Fe- d_{yz} orbitals (labeled in orange in Fig. 1) also form a kagome three-band structure. However, the interaction between the Fe atoms and the p_z orbitals of the Ge^{out} leads to two bands shifting downward away from E_F . Along the $A - L - H - A$ path in the $k_z=0.5$ plane there are three kagome structures. Due to the interaction with the p orbitals of Ge^{out} , the three-band kagome structure composed of Fe- d_{z^2} orbitals is located below and away from the Fermi energy level in the $k_z=0$ plane (from -2.5 to -1.0 eV), while in the $k_z=0.5$ plane the energy bands rise and cross the Fermi level. Two vHSs at the L point close to the Fermi energy level are contributed by Fe- $d_{x^2-y^2}/d_{xy}$ and Fe- d_{z^2} orbitals, marked as vHS2 and vHS3 respectively in Fig. 1 (The analysis below confirms that the vHS2 in $k_z=0$ plane slowly turn into the vHS2 in $k_z=0.5$ plane with k_z shifts from 0 to 0.5). It is worth mentioning that vHSs near E_F have different orbital characters in $k_z=0$ and $k_z=0.5$ planes, indicating the important role of k_z in electronic structures.

Furthermore, using group theory [79, 80], we obtain the

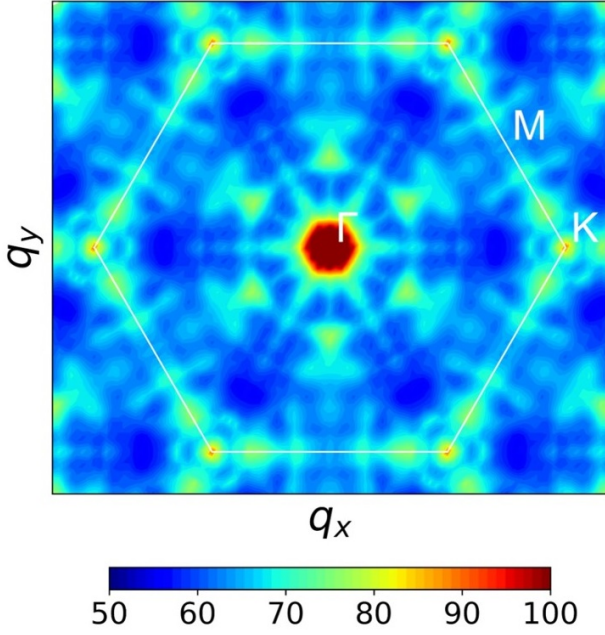


FIG. 2. The nesting function $\xi(q_x, q_y, 0)$ of FeGe. We neglected the peak at $q=0$ to better present the nesting function.

irreducible representations (irreps) of the little group for each vHS based on the wave functions from DFT calculations. At the M point, our calculations identify the irrep of vHS1 as B_{3g} , while vHS2 corresponds to the irrep A_g . On the other hand, at L point, the irrep of the vHS2 and vHS3 are both A_u . The irreps of the vHSs closer to E_F are different in $k_z=0$ and $k_z=0.5$ planes, also indicating the strong 3D feature in FeGe, which will be discussed carefully in the following.

To understand the CDW instability, we calculate the Fermi surface nesting function $\xi(\mathbf{q})$ [81]. The $2 \times 2 \times 2$ supercell structure of CDW phase for the non-magnetic pristine phase is suggested by experimental results [60–63]. Since the A-type AFM structure has already enlarged unit cells doubled along the z -direction, we focus the in-plane \mathbf{q} vector in the following, and obtain the nesting function $\xi(q_x, q_y, 0)$, as is illustrated in Fig. 2. It can be seen that the maximum values of nesting function are located at the K point instead of the M point, which is different from the results of the tight-binding model of kagome lattice [7–10] and AV_3Sb_5 [31, 33]. This motivated a careful analysis of the band structure, Fermi surface and the nesting function of FeGe.

As shown in Fig. 3(a), for $k_z = 0$ plane, the Fermi surface pocket formed by the d_{xz} -dominant energy band (labeled as β) presents a hexagon parallel to the BZ (hereafter called the h-hexagon), and the maximum of nesting function is located at K point (bottom panel of Fig. 3(a)). Differently, the Fermi surface structure in AV_3Sb_5 [31, 33] is v-hexagon, i.e. a hexagon with a difference of 60° rotation from the BZ edge direction, where the peak of nesting function is located at M point. It is worth mentioning that in Fig. 2, besides the maximum of total nesting function located at the K point, there are also peaks along the $\Gamma - M$ direction. Therefore we carefully analyse the k_z momentum-dependent evolution of band

structure, Fermi surface and the nesting function, and show the results in Fig. 3(a-f). As k_z increases from 0 to 0.2, vHS1 gradually approaches the Fermi surface, and the Fermi surface pocket β gradually changes from h-hexagon to v-hexagon as shown in Fig. 3(a-c). The $d_{x^2-y^2}/d_{xy}$ bands forming the pocket α and containing vHS2 shift down as k_z increases, and the shape of the pocket α changes from a v-hexagonal shape (see Fig. 3(c)) to a circle (see Fig. 3(d)), and then gradually to an h-hexagonal shape (see Figs. 3(e) and (f)) as k_z increases. For $k_z=0.5$ plane, the Fermi surface evolved to contain three different h-hexagonal-shaped pockets. As can be seen from Fig. 3, although the shape of the Fermi surface changes with k_z , pockets α and β both retain their hexagonal-like shape for a wide range of k_z values, suggesting a large contribution to the Fermi surface nesting.

For the $k_z = 0$ and 0.1 and planes, the maximum of nesting function are located at or near the K point, as shown in Fig. 3(a) and (b). While in the $k_z=0.2$ plane, the nesting function shows an enhancement along the $\Gamma - M$ direction in the momentum space, as shown in Fig. 3(c), which is originate from the nesting of v-hexagonal pockets α and β in Fig. 3(c). As k_z continues to shift to around 0.4, the shape of the pockets α and β changes again from a v-hexagon to an h-hexagon, with the maximum of nesting function gradually moving away from the $\Gamma - M$ direction to the $\Gamma - K$ direction. For $k_z=0.5$ plane, the h-hexagonal pockets around Γ with similar area to the BZ plane lead to the maxima of the nesting function near the Γ point along the $\Gamma - K$ direction, as shown in Fig. 3(f).

The difference between the Fermi surface and nesting functions of AV_3Sb_5 and that of FeGe origin from their different crystal structures. In AV_3Sb_5 ($A = \text{K}, \text{Cs}, \text{Rb}$), due to the presence of the A layers, the distance between the interlayer V atoms is at least 9.308 \AA . In FeGe, on the other hand, the minimum distance between nearest-neighboring interlayer Fe atoms is 4.041 \AA , since in FeGe only Fe-Ge^{in} and Ge^{out} layers are alternately arranged. Thus, the hopping parameters of Fe-3d orbitals in the z -direction are significantly larger than those of V-d orbitals, and the bands near the Fermi surface in FeGe, which are mainly contributed by Fe-3d orbitals, have strong 3D features.

In tight-binding models of kagome lattice [7–10] and AV_3Sb_5 [30, 31, 33], the vHSs near the Fermi level could induce the peak of nesting at M point. Meanwhile, in AV_3Sb_5 , the phonon instability [30, 33] and the CDW transition [20–25] at M point driven by Fermi surface nesting is suggested. However, in FeGe, where the Fermi surface has strong 3D feature, the vHSs are not always near the Fermi energy level. For example, vHS1 is close to the Fermi level ($\pm 0.1 \text{ eV}$) only in the small range of $k_z=0.183\text{--}0.267$, which is 16.8% of the BZ. Meanwhile, the fraction of k_z when vHS2 and vHS3 are close to the Fermi level are 53.4% and 13.4%, respectively. Our numerical results show that the ratio of nesting function contributed by vHS1, vHS2, and vHS3 around the Fermi level to the total nesting function are 11.02%, 20.44% and 7.53%, respectively. It means that unlike AV_3Sb_5 [30, 31, 33], vHSs near the Fermi surface is not the most important factors of the nesting function in FeGe.

In FeGe, the maximum of nesting function is at the K point,

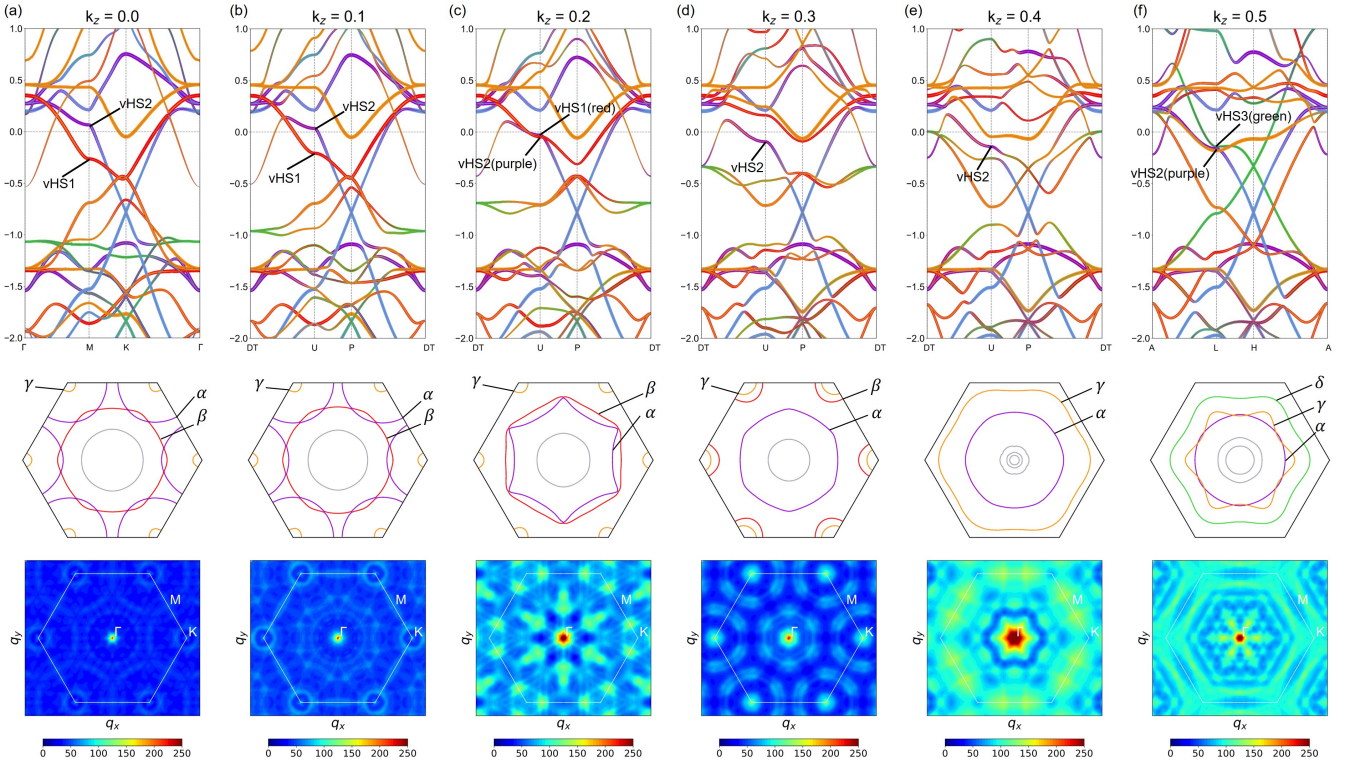


FIG. 3. (a)-(f) The orbital-projected electronic band structures (top panel) and 2D Fermi surface (middle panel), and the nesting function (bottom panel) of FeGe along the $DT(0,0,k_z) - U(\frac{1}{2},0,k_z) - P(\frac{1}{3},\frac{1}{3},k_z) - DT(0,0,k_z)$ path in the $k_z=0, 0.1, 0.2, 0.3, 0.4$, and 0.5 planes. For the orbital-projected band structures, the circle size shows the relative portion of each orbital. The green, purple, blue, red, and orange color represent the $Fe-d_{z^2}$, $Fe-d_{x^2-y^2}$, $Fe-d_{xy}$, $Fe-d_{xz}$, and $Fe-d_{yz}$ characters, respectively. For the 2D Fermi surface, the pockets α , β , γ , and δ represent the pockets dominated by a combination of $Fe-d_{xy}$ and $d_{x^2-y^2}$, $Fe-d_{xz}$, $Fe-d_{yz}$, and $Fe-d_{z^2}$ orbital characters, respectively.

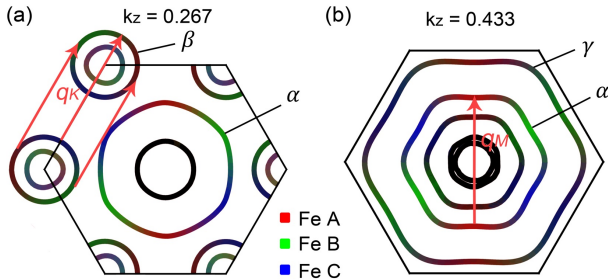


FIG. 4. The 2D Fermi surface in $k_x - k_y$ plane with (a) $k_z=0.267$ and (b) $k_z=0.433$. The sublattice characters of the Fermi level states including three different Fe_A , Fe_B , and Fe_C sites, are marked in yellow, red and blue, respectively. The red arrows indicate the nesting vectors $q_K=(1/3,1/3,0)$ and $q_M=(1/2,0,0)$.

which does not correspond to the observed CDW wave vector at M point, indicating the interaction plays an important role in CDW transition [71]. Meanwhile, the theoretically calculated phonon spectrum remain positive [58, 62, 63]. It implies that the CDW transition is not driven by electron-phonon interaction. Therefore, we analyze the local electron-electron correlation interaction, which is of substantial importance in $3d$ electron systems [82].

Based on DFT calculations, we obtain the wave functions $\psi_{n,\mathbf{k}+\mathbf{q}}(\mathbf{r})$ and $\psi_{n,\mathbf{k}}(\mathbf{r})$, which are electronic Bloch states at the Fermi level connected by the vector \mathbf{q} . We expand the distribution of $\psi_{n,\mathbf{k}+\mathbf{q}}(\mathbf{r})$ and $\psi_{n,\mathbf{k}}(\mathbf{r})$ to the basis set of atomic orbitals in real space. We find that when $\mathbf{q} = \mathbf{q}_K(1/3, 1/3, 0)$, the wave functions $\psi_{n,\mathbf{k}+\mathbf{q}}(\mathbf{r})$ and $\psi_{n,\mathbf{k}}(\mathbf{r})$ are with unequal predominant sublattice occupancy. Meanwhile, when $\mathbf{q} = \mathbf{q}_M(1/2, 0, 0)$, the wave functions $\psi_{n,\mathbf{k}+\mathbf{q}}(\mathbf{r})$ and $\psi_{n,\mathbf{k}}(\mathbf{r})$ are mainly distributed from the same Fe site. We take a representative $k_z=0.267$ plane as an example to show the above mentioned results for the nesting vector \mathbf{q}_K in Fig. 4(a), with the characters of three sublattice Fe_A , Fe_B , and Fe_C indicated in red, yellow and blue, respectively. The Fermi surface contours of β pockets coincide when shifted along the nesting vector $\mathbf{q}_K(1/3, 1/3, 0)$, as shown in red arrows of Fig. 4(a), resulting in the peak of nesting function at K point. However, the nesting vector \mathbf{q}_K connects Fermi surface points with mainly different sublattice occupation, as shown in Fig. 4(a). It is worth mentioning that, due to the locality of Coulomb correlation, the electron-electron correlation interaction is diagonal in the index of atomic sites. It means that the susceptibility is suppressed regardless of the peak of nesting function at K point [71]. Meanwhile, we demonstrate the results of the nesting vector \mathbf{q}_M by $k_z=0.433$ plane in Fig. 4(b). There are

nested Fermi surfaces along $\mathbf{q}_M(1/2, 0, 0)$ connecting the opposite edges of Fermi pocket α , as shown in red arrow of Fig. 4(b). It can be seen that the wave functions $\psi_{n,\mathbf{k}+\mathbf{q}}(\mathbf{r})$ and $\psi_{n,\mathbf{k}}(\mathbf{r})$ connected by the vector \mathbf{q}_M are dominated by same sublattice occupancy as mentioned above, leading to enhanced susceptibility at the M point. Therefore, similar with the sublattice mechanism in superconductors [10, 72], the CDW instability at M point is considered to be derived by the local electron correlation.

I. CONCLUSION

In summary, based on DFT calculations, we comprehensively investigated the electronic structure and Fermi surface nesting in the kagome magnetic metal FeGe. Our results indicate that the energy bands and Fermi surfaces of FeGe vary significantly with k_z , and the maximum of nesting function is at the K point instead of the M point of the CDW instability. We find that the susceptibility at the K point is significantly suppressed due to the sublattice interference mechanism [10, 72], on the other hand the CDW instability at the M point is enhanced, which indicates that the electron correlation plays an indispensable part in the CDW transition.

II. ACKNOWLEDGEMENT

This work was supported by the NSFC (No. 12188101, 11834006, 12004170, 11790311, 51721001), Natural Science Foundation of Jiangsu Province, China (Grant No. BK20200326), and the excellent programme in Nanjing University. Xiangang Wan also acknowledges the support from the Tencent Foundation through the XPLOER PRIZE.

III. APPENDIX

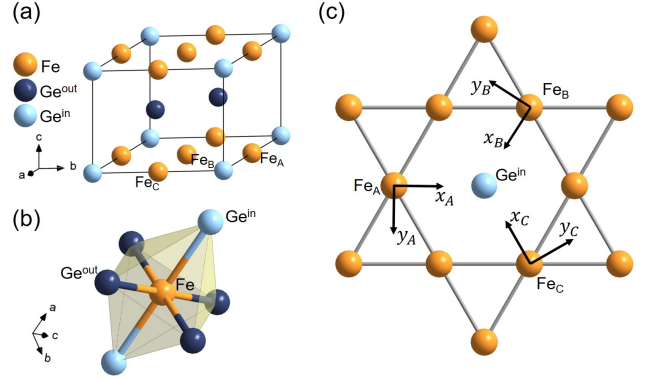


FIG. 5. (a) The crystal structure of FeGe. The light blue, dark blue, and orange spheres represent Ge^{in} , Ge^{out} , and Fe atoms, respectively. The Fe atoms located at three different sites are labeled as Fe_A , Fe_B , and Fe_C . (b) The local structure of the FeGe_6 octahedron. The octahedron includes two Ge^{in} atoms and four Ge^{out} atoms. (c) Our local coordinate for each Fe atom. The local x-axis always points to the nearest-neighbor Ge^{in} atom, and the z-axis of each local coordinate is perpendicular to the paper surface.

A. Crystal Structure

Hexagonal FeGe is an intermetallic compound of the CoSn structure and crystallize into the $P6/mmm$ (No. 191) space group [64]. As shown in Fig. 5(a), there are two distinct types of Ge atoms in a unit cell, labeled Ge^{in} (site 1a) and Ge^{out} (site 2d) respectively, depending on whether they are on the same layer as Fe atoms. In the Fe- Ge^{in} plane, three Fe atoms at different sites (noted as Fe_A , Fe_B , and Fe_C in Fig. 5(a)) form Kagome lattices, and Ge^{in} atoms are located in the center of the hexagons. Ge^{out} atoms compose honeycomb structures above and below the Fe- Ge^{in} plane.

The local structure of the FeGe_6 octahedron is shown in Fig. 5(b). It can be seen that each Fe atom is surrounded by six Ge atomic octahedrons, including two Ge^{in} atoms and four Ge^{out} atoms. In the O_h crystal field, ortho-octahedral structure leads to $t_{2g} - e_g$ energy splitting. Here the octahedron is distorted and induces further splitting of the five Fe-3d orbitals.

B. Band structure and density of states

We perform LSDA calculation for FeGe based on the experimental A-type AFM ground state [70], and show the band structure and the DOS in Fig. 6. As shown in Fig. 6, it is clear that the Fe-3d orbitals dominate the DOS around E_F (-2 to 2 eV relative to E_F), while the Ge-4p orbitals are mainly located between -6.0 and -2.0 eV. In the AFM phase, there is an upshift of the spin minority bands due to the exchange

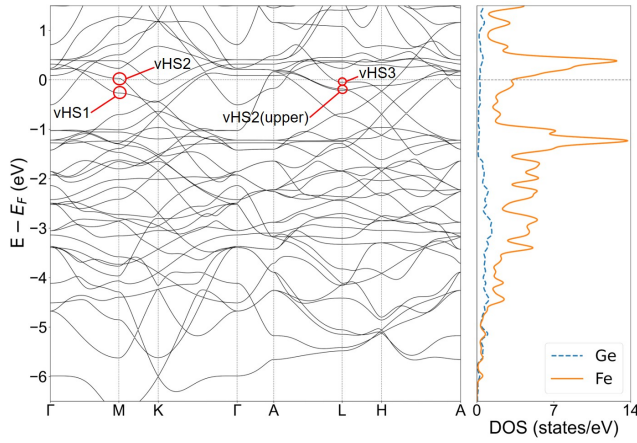


FIG. 6. Band structure (left panel) and DOS (right panel) of A-type AFM FeGe. The Fermi level is aligned to 0 eV. The DOS of Fe-3d orbitals and Ge-4p orbitals are indicated by the solid orange and dashed blue lines, respectively.

splitting induced by the ordered moment. Two peaks located near 0.4 and -1.3 eV correspond to the flat bands of the spin minority and spin majority states, respectively. The contribution of the Fe-3d and Ge-4p orbitals is relatively close in the range from -6 to -4 eV, suggesting hybridization between the Fe-3d and Ge-4p orbitals.

-
- [1] I. Syözi, “Statistics of Kagomé Lattice,” *Prog. Theor. Phys.* **6**, 306–308 (1951).
- [2] J.-X. Yin, B. Lian, and M. Z. Hasan, “Topological kagome magnets and superconductors,” *Nature* **612**, 647–657 (2022).
- [3] H. Chen, B. Hu, Y. Ye, H. Yang, and H.-J. Gao, “Superconductivity and unconventional density waves in vanadium-based kagome materials AV_3Sb_5 ,” *Chin. Phys. B* **31**, 097405 (2022).
- [4] T. Nguyen and M. Li, “Electronic properties of correlated kagomé metals AV_3Sb_5 (A = K, Rb, and Cs): A perspective,” *J. Appl. Phys.* **131**, 060901 (2022).
- [5] A. Mielke, “Ferromagnetic ground states for the Hubbard model on line graphs,” *J. Phys. A: Math. Gen.* **24**, L73 (1991).
- [6] A. Tanaka and H. Ueda, “Stability of ferromagnetism in the Hubbard model on the Kagome lattice,” *Phys. Rev. Lett.* **90**, 067204 (2003).
- [7] M. L. Kiesel, C. Platt, and R. Thomale, “Unconventional Fermi surface instabilities in the kagome Hubbard model,” *Phys. Rev. Lett.* **110**, 126405 (2013).
- [8] T. Park, M. Ye, and L. Balents, “Electronic instabilities of kagome metals: saddle points and Landau theory,” *Phys. Rev. B* **104**, 035142 (2021).
- [9] S.-L. Yu and J.-X. Li, “Chiral superconducting phase and chiral spin-density-wave phase in a Hubbard model on the kagome lattice,” *Phys. Rev. B* **85**, 144402 (2012).
- [10] M. L. Kiesel and R. Thomale, “Sublattice interference in the kagome Hubbard model,” *Phys. Rev. B* **86**, 121105 (2012).
- [11] F. Pollmann, P. Fulde, and K. Shtengel, “Kinetic Ferromagnetism on a Kagome Lattice,” *Phys. Rev. Lett.* **100**, 136404 (2008).
- [12] H.-M. Guo and M. Franz, “Topological insulator on the kagome lattice,” *Phys. Rev. B* **80**, 113102 (2009).
- [13] T.-H. Han, J. S. Helton, S. Chu, D. G. Nocera, J. A. Rodriguez-Rivera, C. Broholm, and Y. S. Lee, “Quantum-limit Chern topological magnetism in TbMn_6Sn_6 ,” *Nature* **583**, 533–536 (2020).
- [14] K. Kuroda, T. Tomita, M.-T. Suzuki, C. Bareille, A. A. Nugroho, P. Goswami, M. Ochi, M. Ikhlas, M. Nakayama, S. Akebi, R. Noguchi, R. Ishii, N. Inami, K. Ono, H. Kuroda, A. Varykhalov, T. Muro, T. Koretsune, R. Arita, S. Shin, T. Kondo, and S. Nakatsuji, “Evidence for magnetic Weyl fermions in a correlated metal,” *Nat. Mater.* **16**, 1090–1095 (2017).
- [15] N. Morali, R. Batabyal, P. K. Nag, E. Liu, Q. Xu, Y. Sun, B. Yan, C. Felser, N. Avraham, and H. Beidenkopf, “Fermi-arc diversity on surface terminations of the magnetic Weyl semimetal $\text{Co}_3\text{Sn}_2\text{S}_2$,” *Science* **365**, 1286–1291 (2019).
- [16] D. F. Liu, A. J. Liang, E. K. Liu, Q. N. Xu, Y. W. Li, C. Chen, D. Pei, W. J. Shi, S. K. Mo, P. Dudin, T. Kim, C. Cacho, G. Li, Y. Sun, L. X. Yang, Z. K. Liu, S. S. P. Parkin, C. Felser, and Y. L. Chen, “Magnetic Weyl semimetal phase in a Kagomé crystal,” *Science* **365**, 1282–1285 (2019).
- [17] J.-X. Yin, S. S. Zhang, G. Chang, Q. Wang, S. S. Tsirkin, Z. Guguchia, B. Lian, H. Zhou, K. Jiang, I. Belopolski, N. Shumiya, D. Multer, M. Litskevich, T. A. Cochran, H. Lin, Z. Wang, T. Neupert, S. Jia, H. Lei, and M. Z. Hasan, “Negative flat band magnetism in a spin-orbit-coupled correlated kagome magnet,” *Nat. Phys.* **15**, 443–448 (2019).
- [18] B. R. Ortiz, L. C. Gomes, J. R. Morey, M. Winiarski, M. Bordelon, J. S. Mangum, I. W. Oswald, J. A. Rodriguez-Rivera, J. R. Neilson, and et al. S. D. Wilson, “New kagome prototype materials: discovery of KV_3Sb_5 , RbV_3Sb_5 , and CsV_3Sb_5 ,” *Phys. Rev. Mater.* **3**, 094407 (2019).
- [19] A. Subedi, “Hexagonal-to-base-centered-orthorhombic 4Q charge density wave order in kagome metals KV_3Sb_5 , RbV_3Sb_5 , and CsV_3Sb_5 ,” *Phys. Rev. Mater.* **6**, 015001 (2022).
- [20] Y.-X. Jiang, J.-X. Yin, M. M. Denner, N. Shumiya, B. R. Ortiz, G. Xu, Z. Guguchia, J. He, M. S. Hossain, X. Liu, J. Ruff, L. Kautzsch, S. S. Zhang, G. Chang, I. Belopolski, Q. Zhang, T. A. Cochran, D. Multer, M. Litskevich, Z.-J. Cheng, X. P. Yang, Z. Wang, R. Thomale, T. Neupert, S. D. Wilson, and M. Z. Hasan, “Unconventional chiral charge order in kagome superconductor KV_3Sb_5 ,” *Nat. Mater.* **20**, 1353–1357 (2021).
- [21] Y.-P. Lin and R. M. Nandkishore, “Complex charge density waves at Van Hove singularity on hexagonal lattices: Haldane-model phase diagram and potential realization in the kagome metals AV_3Sb_5 (A=K, Rb, Cs),” *Phys. Rev. B* **104**, 045122 (2021).

- (2021).
- [22] H. Li, T. T. Zhang, T. Yilmaz, Y. Y. Pai, C. E. Marvinney, A. Said, Q. W. Yin, C. S. Gong, Z. J. Tu, E. Vescovo, C. S. Nelson, R. G. Moore, S. Murakami, H. C. Lei, H. N. Lee, B. J. Lawrie, and H. Miao, "Observation of Unconventional Charge Density Wave without Acoustic Phonon Anomaly in Kagome Superconductors AV_3Sb_5 ($A=Rb, Cs$)," *Phys. Rev. X* **11**, 031050 (2021).
 - [23] C. Mielke, D. Das, J.-X. Yin, H. Liu, R. Gupta, Y.-X. Jiang, M. Medarde, X. Wu, H. C. Lei, J. Chang, P. Dai, Q. Si, H. Miao, R. Thomale, T. Neupert, Y. Shi, R. Khasanov, M. Z. Hasan, H. Luetkens, and Z. Guguchia, "Time-reversal symmetry-breaking charge order in a kagome superconductor," *Nature* **602**, 245–250 (2022).
 - [24] M. M. Denner, R. Thomale, and T. Neupert, "Analysis of Charge Order in the Kagome Metal AV_3Sb_5 ($A=K,Rb,Cs$)," *Phys. Rev. Lett.* **127**, 217601 (2021).
 - [25] L. Nie, K. Sun, W. Ma, D. Song, L. Zheng, Z. Liang, P. Wu, F. Yu, J. Li, M. Shan, D. Zhao, S. Li, B. Kang, Z. Wu, Y. Zhou, K. Liu, Z. Xiang, J. Ying, Z. Wang, T. Wu, and X. Chen, "Charge-density-wave-driven electronic nematicity in a kagome superconductor," *Nature* **604**, 59–64 (2022).
 - [26] W.-S. Wang, Z.-Z. Li, Y.-Y. Xiang, and Q.-H. Wang, "Competing electronic orders on kagome lattices at van Hove filling," *Phys. Rev. B* **87**, 115135 (2013).
 - [27] Y.-X. Jiang, J.-X. Yin, M. M. Denner, N. Shumiya, B. R. Ortiz, G. Xu, Z. Guguchia, J. He, M. S. Hossain, X. Liu, J. Ruff, L. Kautzsch, S. S. Zhang, G. Chang, I. Belopolski, Q. Zhang, T. A. Cochran, D. Multer, M. Litskevich, Z.-J. Cheng, X. P. Yang, Z. Wang, R. Thomale, T. Neupert, S. D. Wilson, and M. Z. Hasan, "Unconventional chiral charge order in kagome superconductor KV_3Sb_5 ," *Nature* **20**, 59–64 (2021).
 - [28] F. H. Yu, D. H. Ma, W. Z. Zhuo, S. Q. Liu, X. K. Wen, B. Lei, J. J. Ying, and X. H. Chen, "Unusual competition of superconductivity and charge-density-wave state in a compressed topological kagome metal," *Nat. Commun.* **12**, 10–15 (2021).
 - [29] Y. Xiang, Q. Li, Y. Li, W. Xie, H. Yang, Z. Wang, Y. Yao, and H.-H. Wen, "Twofold symmetry of c-axis resistivity in topological kagome superconductor CsV_3Sb_5 with in-plane rotating magnetic field," *Nat. Commun.* **12**, 6727 (2021).
 - [30] H. Tan, Y. Liu, Z. Wang, and B. Yan, "Charge Density Waves and Electronic Properties of Superconducting Kagome Metals," *Phys. Rev. Lett.* **127**, 046401 (2021).
 - [31] S. Wu, B. R. Ortiz, H. Tan, S. D. Wilson, B. Yan, T. Birol, and G. Blumberg, "Charge density wave order in the kagome metal AV_3Sb_5 ($A=Cs, Rb, K$)," *Phys. Rev. B* **105**, 155106 (2022).
 - [32] M. Kang, S. Fang, J.-K. Kim, B. R. Ortiz, S. H. Ryu, J. Kim, J. Yoo, G. Sangiovanni, D. D. Sante, B.-G. Park, C. Jozwiak, A. Bostwick, E. Rotenberg, E. Kaxiras, S. D. Wilson, J.-H. Park, and R. Comin, "Twofold van Hove singularity and origin of charge order in topological kagome superconductor CsV_3Sb_5 ," *Nat. Phys.* **18**, 301–308 (2022).
 - [33] J.-G. Si, W.-J. Lu, Y.-P. Sun, P.-F. Liu, and B.-T. Wang, "Charge density wave and pressure-dependent superconductivity in the kagome metal CsV_3Sb_5 : A first-principles study," *Phys. Rev. B* **105**, 024517 (2022).
 - [34] H. Luo, Q. Gao, H. Liu, Y. Gu, D. Wu, C. Yi, J. Jia, S. Wu, X. Luo, Y. Xu, L. Zhao, Q. Wang, H. Mao, G. Liu, Z. Zhu, Y. Shi, K. Jiang, J. Hu, Z. Xu, and X. J. Zhou, "Electronic nature of charge density wave and electron-phonon coupling in kagome superconductor KV_3Sb_5 ," *Nat. Commun.* **13**, 273 (2022).
 - [35] X. Feng, K. Jiang, Z. Wang, and J. Hu, "Chiral flux phase in the Kagome superconductor AV_3Sb_5 ," *Sci. Bull.* **66**, 1384–1388 (2021).
 - [36] K. Jiang, T. Wu, J. Yin, Z. Wang, M. Z. Hasan, S. D. Wilson, X. Chen, and J. Hu, "Kagome superconductors AV_3Sb_5 ($A=K, Rb, Cs$)," *Natl. Sci. Rev.* (2022), 10.1093/nsr/nwac199.
 - [37] X. Feng, Y. Zhang, K. Jiang, and J. Hu, "Low-energy effective theory and symmetry classification of flux phases on the kagome lattice," *Phys. Rev. B* **104**, 165136 (2021).
 - [38] W.-S. Wang, Z.-Z. Li, Y.-Y. Xiang, and Q.-H. Wang, "Competing electronic orders on kagome lattices at van Hove filling," *Phys. Rev. B* **87**, 115135 (2013).
 - [39] H. Chen, H. Yang, B. Hu, Z. Zhao, J. Yuan, Y. Xing, G. Qian, Z. Huang, G. Li, Y. Ye, S. Ma, S. Ni, H. Zhang, Q. Yin, C. Gong, Z. Tu, H. Lei, H. Tan, S. Zhou, C. Shen, X. Dong, B. Yan, Z. Wang, and H.-J. Gao, "Roton pair density wave in a strong-coupling kagome superconductor," *Nature* **599**, 222–228 (2021).
 - [40] B. Ortiz, S. Teicher, Y. Hu, J. Zuo, P. Sarte, E. Schueller, A. Abeykoon, M. Krogstad, S. Rosenkranz, R. Osborn, R. Seshadri, L. Balents, J. He, and S. Wilson, " CsV_3Sb_5 : A Z_2 Topological Kagome Metal with a Superconducting Ground State," *Phys. Rev. Lett.* **125**, 247002 (2020).
 - [41] B. R. Ortiz, P. M. Sarte, E. M. Kenney, M. J. Graf, S. M. L. Teicher, R. Seshadri, and S. D. Wilson, "Superconductivity in the Z_2 kagome metal KV_3Sb_5 ," *Phys. Rev. Mater.* **5**, 034801 (2021).
 - [42] E. Tang, J.-W. Mei, and X.-G. Wen, "High-temperature fractional quantum hall states," *Phys. Rev. Lett.* **106**, 236802 (2011).
 - [43] A. Rüegg and G. A. Fiete, "Fractionally charged topological point defects on the kagome lattice," *Phys. Rev. B* **83**, 165118 (2011).
 - [44] A. O' Brien, F. Pollmann, and P. Fulde, "Strongly correlated fermions on a kagome lattice," *Phys. Rev. B* **81**, 235115 (2010).
 - [45] K. Ohgushi, S. Murakami, and N. Nagaosa, "Spin anisotropy and quantum Hall effect in the kagomé lattice: Chiral spin state based on a ferromagnet," *Phys. Rev. B* **62**, R6065–R6068 (2000).
 - [46] E. Liu, Y. Sun, N. Kumar, L. Muechler, A. Sun, L. Jiao, S.-Y. Yang, D. Liu, A. Liang, Q. Xu, J. Kroder, V. Süß, H. Borrmann, C. Shekhar, Z. Wang, C. Xi, W. Wang, W. Schnelle, S. Wirth, Y. Chen, S. T. B. Goennenwein, and C. Felser, "Giant anomalous Hall effect in a ferromagnetic kagome-lattice semimetal," *Nat. Phys.* **14**, 1125–1131 (2018).
 - [47] A. K. Nayak, J. E. Fischer, Y. Sun, B. Yan, J. Karel, A. C. Komarek, C. Shekhar, N. Kumar, W. Schnelle, J. Kübler, C. Felser, and S. S. P. Parkin, "Large anomalous Hall effect driven by a nonvanishing Berry curvature in the noncollinear antiferromagnet Mn_3Ge ," *Sci. Adv.* **2**, e1501870 (2016).
 - [48] N. Kiyohara, T. Tomita, and S. Nakatsuji, "Giant Anomalous Hall Effect in the Chiral Antiferromagnet Mn_3Ge ," *Phys. Rev. Appl.* **5**, 064009 (2016).
 - [49] S.-Y. Yang, Y. Wang, B. R. Ortiz, D. Liu, J. Gayles, E. Derunova, R. Gonzalez-Hernandez, L. Šmejkal, Y. Chen, S. S. P. Parkin, S. D. Wilson, E. S. Toberer, T. McQueen, and M. N. Ali, "Giant, unconventional anomalous Hall effect in the metallic frustrated magnet candidate, KV_3Sb_5 ," *Sci. Adv.* **6**, eabb6003 (2020).
 - [50] F. H. Yu, T. Wu, Z. Y. Wang, B. Lei, W. Z. Zhuo, J. J. Ying, and X. H. Chen, "Concurrence of anomalous Hall effect and charge density wave in a superconducting topological kagome metal," *Phys. Rev. B* **104**, L041103 (2021).
 - [51] M. Kang, L. Ye, S. Fang, J.-S. You, A. Levitan, M. Han, J. I. Facio, C. Jozwiak, A. Bostwick, E. Rotenberg, M. K. Chan, R. D. McDonald, D. Graf, K. Kaznatcheev, E. Vescovo, D. C. Bell,

- E. Kaxiras, J. van den Brink, M. Richter, M. Prasad Ghimire, J. G. Checkelsky, and R. Comin, “Dirac fermions and flat bands in the ideal kagome metal FeSn,” *Nat. Mater.* **19**, 163–169 (2020).
- [52] Y. Xie, L. Chen, T. Chen, Q. Wang, Q. Yin, J. R. Stewart, M. B. Stone, L. L. Daemen, E. Feng, H. Cao, H. Lei, Z. Yin, A. H. MacDonald, and P. Dai, “Spin excitations in metallic kagome lattice FeSn and CoSn,” *Commun. Phys.* **4**, 240 (2021).
- [53] B. C. Sales, J. Yan, W. R. Meier, A. D. Christianson, S. Okamoto, and M. A. McGuire, “Electronic, magnetic, and thermodynamic properties of the kagome layer compound FeSn,” *Phys. Rev. Mater.* **3**, 114203 (2019).
- [54] S.-H. Do, K. Kaneko, R. Kajimoto, K. Kamazawa, M. B. Stone, J. Y. Y. Lin, S. Itoh, T. Masuda, G. D. Samolyuk, E. Dagotto, W. R. Meier, B. C. Sales, H. Miao, and A. D. Christianson, “Damped Dirac magnon in the metallic kagome antiferromagnet FeSn,” *Phys. Rev. B* **105**, L180403 (2022).
- [55] Y.-F. Zhang, X.-S. Ni, T. Datta, M. Wang, D.-X. Yao, and K. Cao, “Ab initio study of spin fluctuations in the itinerant kagome magnet fesn,” *Phys. Rev. B* **106**, 184422 (2022).
- [56] L. Ye, M. Kang, J. Liu, F. von Cube, C. R. Wicker, T. Suzuki, C. Jozwiak, A. Bostwick, E. Rotenberg, D. C. Bell, L. Fu, R. Comin, and J. G. Checkelsky, “Massive Dirac fermions in a ferromagnetic kagome metal,” *Nature* **555**, 638–642 (2018).
- [57] Z. Lin, J.-H. Choi, Q. Zhang, W. Qin, S. Yi, P. Wang, L. Li, Y. Wang, H. Zhang, Z. Sun, L. Wei, S. Zhang, T. Guo, Q. Lu, J.-H. Cho, C. Zeng, and Z. Zhang, “Flat bands and Emergent Ferromagnetic Ordering in Fe₃Sn₂ Kagome Lattices,” *Phys. Rev. Lett.* **121**, 096401 (2018).
- [58] X. Teng, J. S. Oh, H. Tan, L. Chen, J. Huang, B. Gao, J.-X. Yin, J.-H. Chu, M. Hashimoto, D. Lu, C. Jozwiak, A. Bostwick, E. Rotenberg, G. E. Granroth, B. Yan, R. J. Birgeneau, P. Dai, and M. Yi, “Intertwined magnetism and charge density wave order in kagome FeGe,” *arXiv preprint arXiv:2210.06653* (2022).
- [59] H. Zhou, S. Yan, D. Fan, D. Wang, and X. Wan, “Magnetic interactions and possible structural distortion in kagome FeGe from first-principles study and symmetry analysis,” *arXiv preprint arXiv:2211.15545* (2022).
- [60] X. Teng, L. Chen, F. Ye, E. Rosenberg, Z. Liu, J.-X. Yin, Y.-X. Jiang, J. S. Oh, M. Z. Hasan, K. J. Neubauer, B. Gao, Y. Xie, M. Hashimoto, D. Lu, C. Jozwiak, A. Bostwick, E. Rotenberg, R. J. Birgeneau, J.-H. Chu, M. Yi, and P. Dai, “Discovery of charge density wave in a kagome lattice antiferromagnet,” *Nature* **609**, 490–495 (2022).
- [61] J.-X. Yin, Y.-X. Jiang, X. Teng, M. S. Hossain, S. Mardanya, T.-R. Chang, Z. Ye, G. Xu, M. M. Denner, T. Neupert, B. Lienhard, H.-B. Deng, C. Setty, Q. Si, G. Chang, Z. Guguchia, B. Gao, N. Shumiya, Q. Zhang, T. A. Cochran, D. Multer, M. Yi, P. Dai, and M. Z. Hasan, “Discovery of Charge Order and Corresponding Edge State in Kagome Magnet FeGe,” *Phys. Rev. Lett.* **129**, 166401 (2022).
- [62] H. Miao, T. T. Zhang, H. X. Li, G. Fabbri, A. H. Said, R. Tartaglia, T. Yilmaz, E. Vescovo, J.-X. Yin, S. Murakami, L. X. Feng, K. Jiang, X. L. Wu, A. F. Wang, S. Okamoto, Y. L. Wang, and H. N. Lee, “Spin-Phonon Coupling Driven Charge Density Wave in a Kagome Magnet,” *arXiv preprint arXiv:2210.06359* (2022).
- [63] S. Shao, J.-X. Yin, I. Belopolski, J.-Y. You, T. Hou, H. Chen, Y.-X. Jiang, M. S. Hossain, M. Yahyavi, C.-H. Hsu, Y. Feng, A. Bansil, M. Z. Hasan, and G. Chang, “Charge density wave interaction in a Kagome-honeycomb antiferromagnet,” *arXiv preprint arXiv: 2206.12033* (2022).
- [64] T. Ohoyama, K. Kanematsu, and K. Yasukōchi, “A New Intermetallic Compound FeGe,” *J. Phys. Soc. Jpn.* **18**, 589–589 (1963).
- [65] O. Beckman, K. Carrander, L. Lundgren, and M. Richardson, “Susceptibility Measurements and Magnetic Ordering of Hexagonal FeGe,” *Phys. Scr.* **6**, 151 (1972).
- [66] L. Häggström, T. Ericsson, R. Wäppling, and E. Karlsson, “Mössbauer Study of Hexagonal FeGe,” *Phys. Scr.* **11**, 55 (1975).
- [67] U. Gäfvert, L. Lundgren, B. Westerstrandh, and O. Beckman, “Crystalline anisotropy energy of uniaxial antiferromagnets evaluated from low field torque data,” *J. Phys. Chem. Solids* **38**, 1333–1339 (1977).
- [68] J. B. Forsyth, C. Wilkinson, and P. Gardner, “The low-temperature magnetic structure of hexagonal FeGe,” *J. Phys. F: Metal Phys.* **8**, 2195 (1978).
- [69] J. Bernhard, B. Lebech, and O. Beckman, “Neutron diffraction studies of the low-temperature magnetic structure of hexagonal FeGe,” *J. Phys. F: Metal Phys.* **14**, 2379 (1984).
- [70] J. Bernhard, B. Lebech, and O. Beckman, “Magnetic phase diagram of hexagonal FeGe determined by neutron diffraction,” *J. Phys. F: Metal Phys.* **18**, 539 (1988).
- [71] S. Doniach and E. H. Sondheimer, *Green’s Functions for Solid State Physicists* (1998).
- [72] X. Wu, T. Schwemmer, T. Müller, A. Consiglio, G. Sangiovanni, D. D. Sante, Y. Iqbal, W. Hanke, A. P. Schnyder, M. M. Denner, M. H. Fischer, T. Neupert, and R. Thomale, “Nature of Unconventional Pairing in the Kagome Superconductors AV₃Sb₅ (A = K, Rb, Cs),” *Phys. Rev. Lett.* **127**, 177001 (2021).
- [73] P. Blaha, K. Schwarz, F. Tran, R. Laskowski, G. K. H. Madsen, and L. D. Marks, “WIEN2k: An APW+lo program for calculating the properties of solids,” *J. Chem. Phys.* **152**, 074101 (2020).
- [74] S. H. Vosko, L. Wilk, and M. Nusair, “Accurate spin-dependent electron liquid correlation energies for local spin density calculations: a critical analysis,” *Can. J. Phys.* **58**, 1200 (1980).
- [75] G. Kresse and J. Hafner, “Ab initio molecular dynamics for liquid metals,” *Phys. Rev. B* **47**, 558(R) (1993).
- [76] G. Kresse and J. Furthmüller, “Efficient iterative schemes for ab initio total-energy calculations using a plane-wave basis set,” *Phys. Rev. B* **54**, 11169 (1996).
- [77] P. E. Blüchl, “Projector augmented-wave method,” *Phys. Rev. B* **50**, 17953 (1994).
- [78] G. Kresse and D. Joubert, “From ultrasoft pseudopotentials to the projector augmented-wave method,” *Phys. Rev. B* **59**, 1758 (1999).
- [79] C. J. Bradley and A. P. Cracknell, *The Mathematical Theory of Symmetry in Solids: Representation Theory for Point Groups and Space Groups*, (Oxford University Press, 1972).
- [80] F. Tang and X. Wan, “Exhaustive construction of effective models in 1651 magnetic space groups,” *Phys. Rev. B* **104**, 085137 (2021).
- [81] M. D. Johannes and I. I. Mazin, “Fermi surface nesting and the origin of charge density waves in metals,” *Phys. Rev. B* **77**, 165135 (2008).
- [82] M. Imada, A. Fujimori, and Y. Tokura, “Metal-insulator transitions,” *Rev. Mod. Phys.* **70**, 1039–1263 (1998).